Journal of the Mechanical Behavior of Biomedical Materials 99 (2019) 93–103

Contents lists available at ScienceDirect

Journal of the Mechanical Behavior of Biomedical Materials

journal homepage: www.elsevier.com/locate/jmbbm

Miniature CoCr laser welds under cyclic shear: Fatigue evolution and crack growth

M. Kanerva[a,b,*], Z. Besharat[c], T. Pärnänen[b], J. Jokinen[a], M. Honkanen[a], E. Sarlin[a], M. Göthelid[c], D. Schlenzka[b]

[a] Tampere University, Faculty of Engineering and Natural Sciences, P.O.Box 589, FI-33014, Tampere, Finland
[b] Orton Orthopaedic Hospital and Research Institute Orton, FI-00280, Helsinki, Finland
[c] Royal Institute of Technology, Surface and Corrosion Science, P.O.Box 10044, SE-16440, Stockholm, Sweden

ARTICLE INFO

Keywords:
CoCr
Implant
Fatigue
Crack growth
Laser weld

ABSTRACT

Miniature laser welds with the root depth in the range of 50–300 μm represent air-tight joints between the components in medical devices, such as those in implants, growth rods, stents and various prostheses. The current work focuses on the development of a fatigue test specimen and procedure to determine fatigue lives of shear-loaded laser welds. A cobalt-chromium (CoCr) alloy is used as a benchmark case. S–N graphs, damage process, and fracture surfaces are studied by applying x-ray analysis, atomic force microscopy, and scanning electron microscopy both before and after the crack onset. A non-linear material model is fitted for the CoCr alloy to run finite element simulations of the damage and deformation. As a result, two tensile-loaded specimen designs are established and the performance is compared to that of a traditional torque-loaded specimen. The new generation specimens show less variation in the determined fatigue lives due to well-defined crack onset point and, therefore, precise weld seam load during the experiments. The fatigue damage concentrates to the welded material and the entire weld experiences fatigue prior to the final, fracture-governed failure phase. For the studied weld seams of hardened CoCr, a regression fatigue limit of 10.8–11.8 MPa, where the stress refers to the arithmetic average shear stress computed along the region dominated by shear loading, is determined.

1. Introduction

Fatigue in biomaterials is a crucial issue when developing medical devices for long-term operation. The great need for reliable fatigue data, common design practice of partly ignoring fatigue evolution, and the lack of in-depth research have been reported (Antunes and De Oliveira, 2012). Likewise, Marrey et al. (Marrey et al., 2006) stressed the inadequacy of current design procedures for the testing of survival instead of actual fatigue design. The more complex and larger structure is being developed, the more challenges fatigue is expected to incur. Limb lengthening implants represent the most complex, largest and difficult metal technologies implantable for human skeleton. Due to the recent progress in the development of autonomous and electrically actuated limb lengthening implants, intramedullary fixation of telescopic implants inside the bone cavity of femur or tibia has become a standard (Baumgart et al., 2005; Thonse et al., 2005; Okyar and Bayoglu, 2012). The intramedullary-fixed implants are made of stainless steel, cobalt-chromium (CoCr) and titanium alloys to reach the extremely high requirements for strength and fatigue life per product. However, the sheer size of patient's bones limits the cavity, i.e., the available space for the implant and complications due to material failure have been reported even for the latest models—one of the main causes was the failure of the metallic shell structure (Tiefenboeck et al., 2016; Calder et al., 2017; Bhat et al., 2006). Similar fatigue requirements exist for polymeric medical products (Scholz et al., 2018).

As a starting point, optimized CoCr alloys are ductile and can form a reliable basis for a shell structure of a hollow, thin-walled prosthesis, stent or a dental bridge and can well be suited to shield patients from peri-implant bone stresses and fatigue micro-mechanisms (Limmahakhun et al., 2017; Al Jabbari et al., 2014; Mani et al., 2007). In turn, laser welding is a viable option to produce complex, durable and air-tight joints in sub millimetre-sized CoCr components (Bertrand et al., 2001; Kanerva et al., 2015). The mechanical strength of the CoCr alloy in laser-welded seams depends on the welding parameters, such as the laser power, pulse time, spot configuration and the heat treatments done on the parent material (Baba et al., 2004; Watanabe et al., 2005).

The reported mechanical characterisation of CoCr in the current literature focuses on quasi-static torque and tensile strength as well as

* Corresponding author. Tampere University, Faculty of Engineering and Natural Sciences, P.O.Box 589, FI-33014, Tampere, Finland.
E-mail address: Mikko.Kanerva@tuni.fi (M. Kanerva).

https://doi.org/10.1016/j.jmbbm.2019.07.004
Received 2 November 2018; Received in revised form 26 June 2019; Accepted 7 July 2019
Available online 10 July 2019

tensile fatigue (Zupancic et al., 2006; Srimaneepong et al., 2008). Miniature welds between robust implant components or prosthesis components are often shear-loaded due to the torsional muscle forces in limbs upon walking or standing up. Macroscopic fatigue tests with partial shear loading are typical for welded lap-joints and studs (Radaj, 1990; Chang et al., 2001) yet they do not give precise information of the damage evolution and fatigue process that is needed for design of miniature structures (Antunes and De Oliveira, 2012; Ladani and Dasgupta, 2009). Development of a test method for miniature CoCr laser welds could lead to a method that can be used to understand the effects of weld surface modification (Hryniewicz et al., 2008) and in-vitro conditions on the fatigue crack nucleation and long-term durability—noting that the biocompatibility of CoCr has been found processing-dependent (Hedberg et al., 2014; Al Jabbari et al., 2014).

In this study, we pursue to characterise a new specimen design for analyzing miniature laser welds and surface crack nucleation under shear loads. The work focuses on specific medical-grade CoCr alloy and its fatigue response in miniature laser weld seams. The outcome is first-ever published fatigue data of shear-loaded CoCr laser welds and crack onset characteristics for CoCr laser welds provided by the new test procedure. The damage evolution analysis is supported by in-depth microscopy and finite element simulation of crack-tip energy release rates and mode-mixity.

2. Material and methods

2.1. CoCr raw material

The raw material cobalt-chromium alloy was supplied by Carpenter Technology (USA) in extruded, strain-hardened bar form. These bars had as-shipped hardness of 47 HRC and they were heat-treated after arrival by Sten & Co Oy Ab (Finland) according to the standard requirements for MP35N (see general aspects in ASTM F562). The parts were cut using electrical discharge machining (EDM) by Mectalent Ltd (Finland). Test specimens were prepared for three different purposes: (1) quasi-static tensile testing for material properties and material modelling; (2) traditional fatigue tests under torque; (3) new test specimen development. The fatigue test specimens were passivated by using a typical procedure for medical CoCr parts and surface-finished before the laser welding in a clean room condition, as described in Table 1.

2.2. Tensile testing for material characterisation

The tensile tests were carried out according to the standard (ASTM E8/E8M–09, 2009) and the miniature dog-bone specimen geometry was applied with dimensions 90 mm × 10 mm × 3 mm, 6 mm ($l \times w \times t$, width at gauge section). A servo-hydraulic test machine (Dartec, 100 kN) with a computerized control (Elite Suite, MTS) and hydraulic grippers was used at a constant displacement rate of 2.0 mm/min. Strain gauges with gauge lengths of 5 mm and 1 mm were fixed to the specimen gauge section to record axial and transverse strain, respectively, as shown in Fig. 1. Four specimens were used for Poisson's ratio determination (two orthogonal gauges necessary per specimen). The area of the failure cross-section was used for the true ultimate stress calculation (Fig. 1).

Table 1
The surface treatment and clean room surface finishing procedure for CoCr parts prior to laser welding in this study.

Step	Procedure	Medium	Time	Environment
1	Degrease	Detergent (Teho A)	12 h	Industrial
2	Rinsing	Water	- -	Industrial
3	Ultrasonic cleaning	Detergent (RMC 3)	5 min	Industrial
4	Rinsing	Water	- -	Industrial
5	Passivation	H_2O + HNO_3, 20–45%	1 h	Industrial
6	Ultrasonic cleaning	Detergent (RMC 3)	5 min	Industrial
7	Rinsing	Water	- -	Industrial
8	Ultrasonic cleaning	Isopropyl alcohol	5 min	Clean room
9	Ultrasonic cleaning	De-ionized water	15 min	Clean room

2.3. Welded fatigue specimens and test setup

The geometries of the traditional as well as the two candidate specimen designs are described in Fig. 1. The traditional specimen is a torque loaded specimen where shearing force along the weld seam is exerted. Due to the material discrepancy and heat-affected zone formed at the weld start and end point in the traditional specimen, the new designs (new generation 'GE' series) were selected to be tensile-loaded, 4.0 mm thick, specimens. The specimens were provided with a stepped lap to separate crack onset and the fatigue damage due to shear. The detailed drawings of the test specimens are given in Appendix A.

The GE1 design represents a geometry that is simple to manufacture (straight edges), thus, is expected to incur less manufacture deviation. The GE2 design targets to a more even energy release distribution due to higher strain at the curved, slender gauge section.

2.3.1. Welding

The fatigue test specimens were surface treated (Table 1) and welded by Mectalent Ltd. (Finland). Precise welding fixtures were prepared for the torque and tensile specimens. The specimen welding was started by fixing the two specimen halves by local weld spots, in order to hold the two halves correctly aligned and to minimize specimen warping due to local (asymmetric) thermal expansion. A single parameter set was used to weld all the specimens. The specimen movement was automatized by using the control stage of the welding device and the speed was set to be equal for the rotational welding (traditional specimens) and the translational welding (GE series). A welding voltage of 175 V was used to form a 0.4 mm beam (diameter) and a pulsed welding was applied at a 5.5 Hz frequency with a pulse duration of 3 ms.

2.3.2. Fatigue testing

The fatigue tests were performed using a testing machine (Electropuls E 3000, Instron) with a 3 kN load cell and computerized control (WaveMatrix, Instron). A sinusoidal loading wave form was applied with a constant min/max peak load ratio of $R_L = 0.1$. The Electropuls tester is capable of controlling independently torque and axial displacement (load) and, hence, the control parameters used for adjusting torque and axial load per programme are given in Table 2. The test machine was adjusted to the specimen stiffness prior to each test by using the automatic tune; each tune was run until the planned fatigue cycle peak load. The specimens were connected using a shaft through the specimen tab area to allow for free rotation during the test and depending on the changes in stiffness along with fatigue. Typical S–N data fitting was made using a power-law regression $N = C \cdot \tau^m$, where τ is the (shear) stress value, and C and m are fitting parameters; the number of cycles (N) was used as a dependent variable.

2.4. Characterisation

Fracture surfaces of the test specimens (after static and fatigue loading) were imaged using scanning electron microscopes (SEM) (models XL 30 Series, FEI/Philips, and Ultra 55, Zeiss). SEM imaging was carried out directly without additional coatings or treatments on samples. The composition of the parent material and weld seam were analysed using an x-ray energy dispersive spectroscopy (EDS) by using an integrated analyser EDS X-Max SDD (Silicon Drift Detector) in the SEM instrument.

Atomic force microscopy (AFM) was used to study the surfaces and crack nucleation in the laser weld seam of the fatigue specimens. An

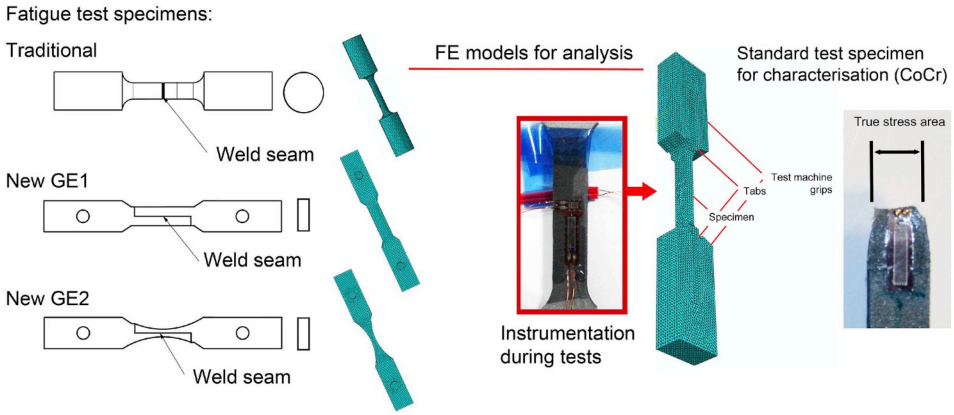

Fig. 1. Standard torque specimen and suggested new geometries (GE1 and GE2) for fatigue testing of miniature laser welds under shear loading; FE models that were created for the numerical analysis are included to indicate the mesh density. The instrumentation of a tensile test specimen for standard material testing is shown with the typical failure mode and the definition of cross-section for true stress calculation.

Table 2
General parameters for test programmes.

Step	Loading phase	Parameters (rate or limit)
Torque cycles		
0	Stiffness tune	Automatic rate, until the cycle peak level
1	Tensile	1 mm/min till −5 N (held)
1	Torque (ramp)	0.1 Nm/min until the mean load level
2	Torque (sinusoidal)	2 Hz, $R_L = 0.1$
Tensile cycles		
0	Stiffness tune	Automatic rate, until the cycle peak level
1	Torque	(0.1 Nm/min until 0.2 Nm (held))
1	Tensile (ramp)	50 N/min, until the mean load level
2	Tensile (sinusoidal)	2 Hz, $R_L = 0.1$

AFM instrument Dimension Icon (Bruker) was used. The measurements were carried out in the tapping mode. Single cantilever probes (μmasch NSC15/AlBS, force constant 40 N/m, tip radius 8 nm) were used. The analysis of metal surfaces prior to fatigue testing was carried out so that a higher-order background was extracted to analyse the nano scale surface morphology.

2.5. Numerical computing

The test specimens were modelled and simulated using *Abaqus*® 2017 (Simulia). Full 3-D finite element (FE) models were generated to account for asymmetric deformation during the simulated test loading (for welded specimens). The test specimen geometry was imported by using the original CAD models. Tabs and test machine interfaces were modelled for the tensile specimen in order to simulate representative load introduction and to ensure a valid fitting of the material model.

2.5.1. Material modelling for CoCr

The tensile specimen (see Section 2.2) material was defined using the ideal-plastic material model in *Abaqus* with four yield points. The ideal plastic model used in this study is based on the division of strain rate into elastic and plastic components, $d\varepsilon = d\varepsilon^e + d\varepsilon^p$. The yield condition was set based on the deviatoric part ($\boldsymbol{S}$) of Cauchy stress ($\boldsymbol{\sigma}$):

$$\boldsymbol{S} = \boldsymbol{\sigma} + p\boldsymbol{I} \quad , \tag{1}$$

where $p = -(\text{trace}[\boldsymbol{\sigma}])/3$ and $\boldsymbol{I}$ is the identity tensor. The plastic strain requirement was presumed to satisfy a uniaxial stress-plastic strain relationship so that a Mises-equivalent scalar stress value could be applied. The specimen was meshed using linear tetrahedrons (C3D4) with an approximate size of 1 mm. Local strains were collected from the elements located at the strain gauges in real specimens (see Fig. 1). The axial and transverse strain (mean over the element centroid values) were compared with the experimental data and the material model was updated until a feasible fit was achieved.

2.5.2. Welded specimen simulation

The traditional specimen and the proposed specimen geometries (GE1 and GE2) were created by composing two specimen halves together (see Fig. 1) and the assembly was designated to the material model fitted for the CoCr alloy. The specimens were meshed using linear bricks (C3D8R) with an approximate size of 0.1 mm to account for accurate stress-strain gradients. The weld was modelled using a contact definition and the fracture along the weld seam was simulated by using the Virtual Crack Closure Technique (VCCT). The use of contact and VCCT means that the process zone at the crack tip was homogenized, thus, defined by the critical energy release rate (ERR) per each nodal release (Krueger, 2004). Since VCCT is based on the assumption of linear force-separation law at a crack tip, the growth of crack was not simulated for the non-linear material in this study. Instead, different lengths of crack at the weld seam were manually created and the ERR values per fracture mode were computed—simulating the positive loading phase of a fatigue test cycle. Poisson's ratio of 0.3 was applied throughout the models and the exact yield points of the elastic-plastic model are given in a previous study (Kanerva et al., 2015).

3. Results and analysis

3.1. Tensile behavior and CoCr material model

The test data from the quasi-static tensile tests resulted in the following tensile properties: the Young's modulus value was determined to be 216 ± 6 GPa (mean over six specimens), Poisson's ratio 0.288 ± 0.01 (mean over four specimens), yield stress at 0.2% permanent deformation 1869 ± 36 MPa (mean over four specimens), and the ultimate true stress 2466 ± 167 MPa (mean over three specimens). In the event of specimen necking under the gauge, leading to subsequent gauge failure, the strain data was not used for the yield stress determination. Similarly, in the event of major tab failure near the test machine gripping, the data was not used for ultimate (failure) stress determination.

The CoCr material model was fitted using four yield points selected based on the experimental stress-strain curve, as shown for the final selection in Fig. 3(a). During the fitting process, the yield point selection was iterated until the simulated specimen behavior matched the experimental data in terms of axial and transverse strain and the final results are shown in Fig. 3(b).

3.2. Fatigue tests under shear

To compare standard torque-loaded specimen and new tensile-loaded specimen geometries, the von Mises (vM) stress at the weld line was determined by the FE analysis (FEA) for three load levels per specimen type. The exact vM stress per particular test peak load was

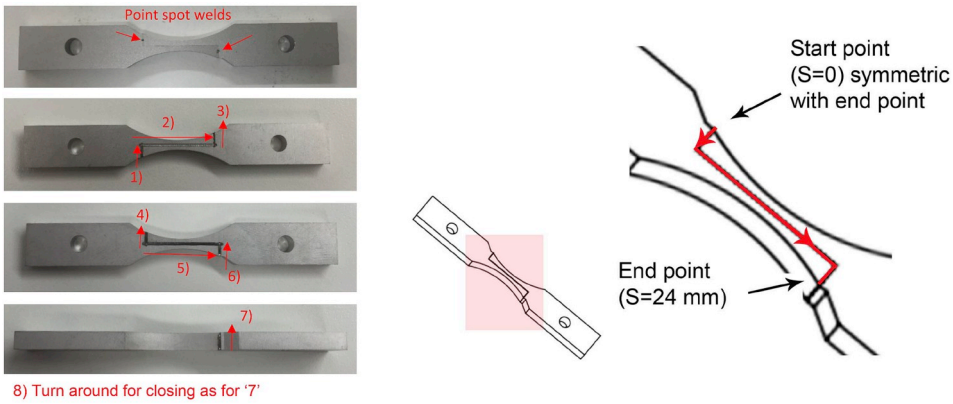

Fig. 2. The welding procedure for GE1 and GE2 specimens and the definition of the *S*-coordinate along the weld line for both GE specimens.

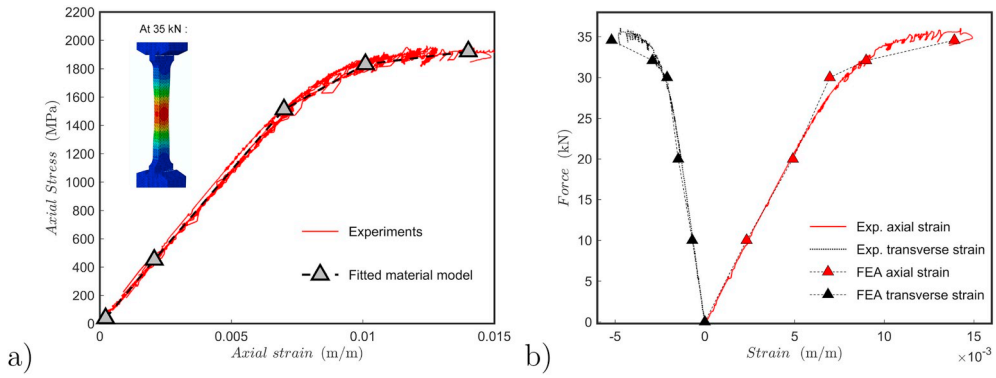

Fig. 3. Finite element simulation based material model fitting: a) selected yield points; b) simulated axial and transverse strain with comparison to tensile test data.

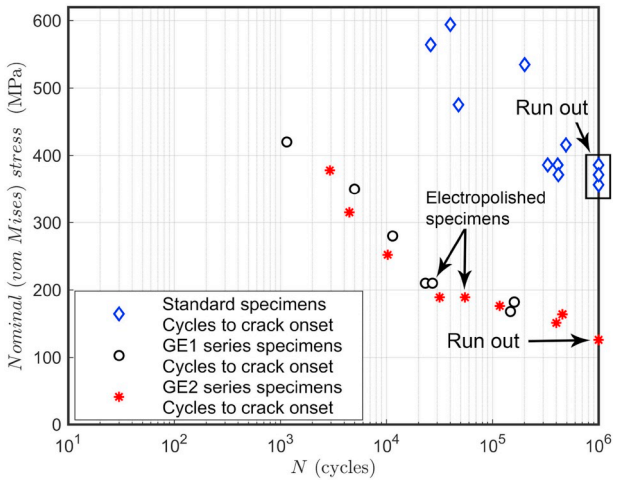

Fig. 4. S–N data for all the specimen designs in terms of total cycles to crack onset.

calculated via linear relation (297 MPa/Nm, 140 MPa/kN, 126 MPa/kN for the standard, GE1 and GE2 specimens, respectively). For GE1 and GE2 specimen, the representative vM stress was an average along the elements in the thickness direction (the crack onset line, i.e. point 7 in Fig. 2) and at the fatigue cycle peak.

The standard specimen has the disadvantage that the exact fatigue limit cannot be clearly determined; the specimen either fails with more or less unpredicted way or does not fail ('run out' testing extended to two million cycles). Naturally, the start and end points of the welding process form a deviation in the material properties and works as a crack initiation point, which is difficult to control accurately. Besides, the weld spot to fix the specimen halves lies along the main weld line. Most importantly, the nominal stress values lead to highly un-conservative designs in reality since the determination of a fatigue limit, even when presuming proper margin of safety, tend to be associated with a very high shear stress level (in the order of 400 MPa in this study).

The computed shear stress distributions in the developed GE test specimens for three load levels are shown in Fig. 5. In general, the shear stress peaks near the weld corners and decreases towards the central specimen. In order to designate a nominal, design stress value, the arithmetic mean shear stress was calculated 1) over the entire distribution, and alternatively 2) over the 'shear part' of the weld (3–21 mm values of the S-coordinate, Fig. 2). The mean values were calculated for the three load levels to form a general rule between the stress level and test load. The mean values clearly agree (as shown in Fig. 6) with a linear relation. For the GE1 specimen, slopes of 13.5 MPa/kN and 9.84 MPa/kN were fitted with a correlation of R^2 = 0.999992 and R^2 = 0.999993, for the shear part values and entire weld seam, respectively. For the GE2 specimen, slopes of 12.8 MPa/kN and 5.75 MPa/kN were fitted with a correlation of R^2 = 0.999997 and R^2 = 0.999994, for the shear part values and entire weld seam, respectively. The fitted slopes related to the values over the shear part represented the load condition of the main test phase and were selected to be used for forming the S–N graphs of the CoCr laser welds.

The fatigue testing results of the GE1 and GE2 specimens are presented in Figs. 4 and 7. The fatigue process of both GE specimens is more diverse compared to the standard torque specimen. The fatigue process can be divided into three distinguishable phases: 1) the crack onset, 2) weld seam fatigue under shear, and 3) final failure. Due to inevitable, natural deviation in the material microstructure, the crack initiates always (first) at one end of the weld line. Due to the strong crack-opening stress, the first 5 mm of weld open in a rather immediate manner with the open crack tip reaching the corner point of the

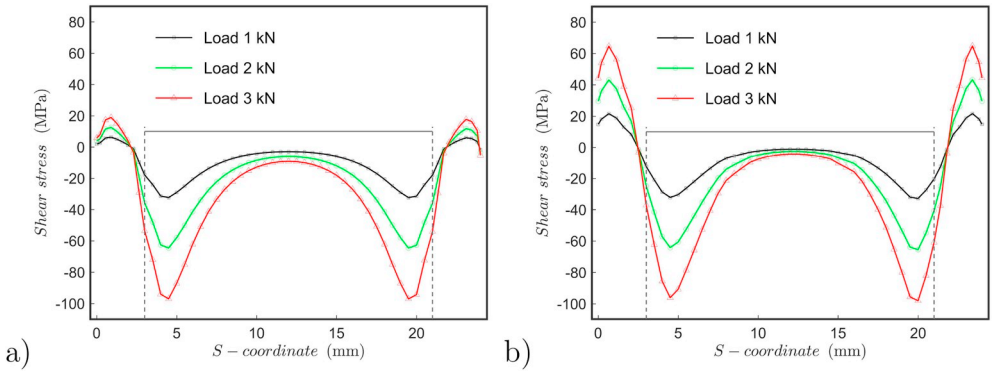

Fig. 5. Computed shear stress distributions in the laser welds for different levels of tensile load: a) GE1 specimen; b) GE2 specimen. Each data point represents the centroid value of the element tied at the modelled weld seam (element width 100 μm at contact). Gray lines are showing the shear load dominated part along *S*-coordinate.

specimen. The crack forms a natural stress singularity point and focuses the fatigue damage right to the miniature weld seam. Both GE1 and GE2 specimens behave in a similar manner in terms of the crack onset related fatigue life, as is expected based on the simulated vM peak stresses.

The actual fatigue life of the laser weld under shearing load was determined based on the cycle count between the point when the crack reached the corner point ('onset') and the final failure. The GE1 specimen was observed to behave somewhat unsatisfactory; once a crack halted to the corner point (near the fatigue limit load) and another crack onset towards the parent material instead of along the weld (at 986 658 total cycles). The GE specimen geometries are scalable in the thickness direction and high enough thickness should be provided per (bulk) specimen to decrease stresses in the parent material. FEA of the GE specimens (Kanerva et al., 2019) showed that the GE1 specimen geometry induces higher peak stresses in the parent material after the crack onset compared to the GE2 specimens due to the differences in the stress-strain gradient around the onset point and due to the different specimen stiffness.

The specimen candidate GE2 was observed to behave in a predictable way and resulted in data point sets producing a gradual turn towards an asymptote, determining the fatigue limit. GE2 series results were used for a power law defined S–N curve fit (correlation of R^2 = 0.989), which finally gives a conservative fatigue limit estimate of 10.8–11.8 MPa (i.e. stress-range for 3–2 million cycles, respectively).

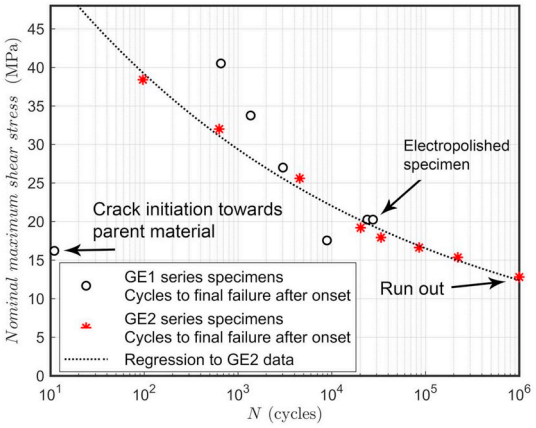

Fig. 7. S–N data covering the cycles to failure along the shear-loaded part of the specimen; data of the GE1 and GE2 specimen series. Cycle count was started after the crack onset in the data of the graph. The fitted S–N curve represents a power law ($N = C \cdot \tau^m$) and has a correlation of R^2 = 0.989 with the GE2 data (C = 6E+14, m = -8.0082).

3.3. Fracture surface morphology

The overall appearance of the welds in standard and GE specimens is illustrated in Fig. 8. The weld depth for all the specimens was approximately 100 μm. The weld quality in terms of voids and constant depth was high, except at the initial spot welds and occasionally near the weld corners of GE specimens. Images in Figs. 9 and 10 are showing details of the fracture surfaces in GE2 specimen after fatigue loading. The crack initiates at the top of the specimen, fast opens and the crack reaches the corner (S ≈ 3 mm) on both sides of the specimen.

For the GE2 specimen series, the crack typically onset at one end of the specimen. Interestingly, the fatigue damage along the shear part (S ≈ 3–21 mm) initiates at the root region of the weld as a long transverse front (see Fig. 9). The root of the laser weld (in the space between the specimen halves) is presumed to have lower mechanical performance because of impurities and/or carbides that form an initiation point of fatigue cracks. According to the periodic striations on the fracture surfaces, fatigue damage evolves towards the weld surface from inside

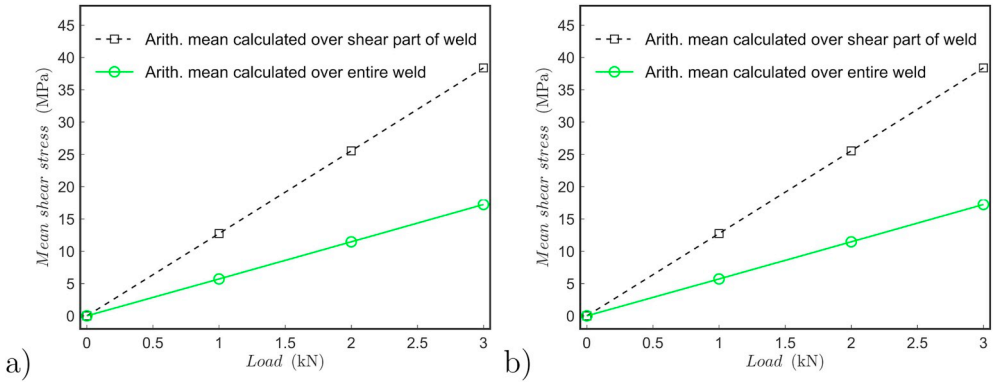

Fig. 6. Linear fitted load-mean shear stress curve slopes: a) GE1 specimen; b) GE2 specimen. The shear part of the weld refers to the range of 5–21 mm values of the *S*-coordinate along the weld seam.

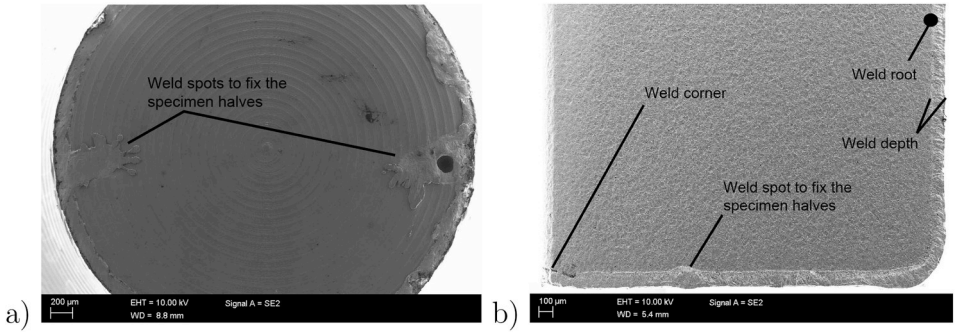

Fig. 8. Overall SEM imaging of the weld fracture surfaces: a) standard specimen after static torque test; b) GE2 specimen after fatigue failure (crack initiation region shown).

the test specimen. Finally, after only a few micron thick skin remains, the crack fully opens and the crack tip (as observed by a test operator) propagates towards the central specimen.

The final failure occurs when the intact weld portion in front of the crack tip (or between the crack tips for symmetric crack propagation) reaches the shear strength of the weld material. On one side (either right or left) where fatigue damage was observed less evolved, the fracture surface resembled ductile fracture under quasi-static failure, with strong shearing ridges and possible contact within the final breakage, as shown in Fig. 10(b).

3.3.1. Elemental composition and sample preparation effects

Selected specimens were used for detailed analysis and, therefore, the central region of these specimens was electropolished. Electropolishing (EP) processes are highly sensitive to the inevitable deviation in solution concentration, exact current density, and quality of rinsing when finishing the treatment (methodology basics given e.g. in Hryniewicz et al. (2008); Lee and Lai (2003)). It is expected that the surface structure on a nano scale varies between the selected specimens. In general, the polishing removes large-scale roughness (above ≈100 nm) but usually does not vary the nano scale structure of the surfaces essentially (see Fig. 11 (b)–(c)). Here, SEM imaging shows qualitatively negligible differences in the *macroscopic* surface roughness of EP specimens.

On a nano scale, the mass removal reaction resulted in a population of pits that are observable in the AFM height data; the phase-difference data being insensitive to variation in sole topology. The change in the surface formation can be traced to the border between the weld seam root and the virgin parent material (Fig. 12). The change in the surface morphology is rather discrete, which indicates fast cooling of the melt after the passing laser within welding and leading to changes in the oxide layer. The results of the elemental analysis are reported by Kanerva et al. (2019). It was verified that there is no radical change in the composition due to either welding or EP treatment. In detail, it could be argued that the welding process tends to lead only in minor chromium depletion on the surface.

3.3.2. Fatigue damage process

Fatigue damage concentrates in to the miniature laser weld due to the bulky structure of the surrounding test specimen. It is important to study the nature and localization and extend of damage in the weld seam. The analysis of the fatigue damage process on the outer weld surface was carried out by measuring surfaces after the removal of specimens from the test machine (right after crack onset). SEM imaging indicates that the fatigue damage occurs at the immediate vicinity of the weld seam (damage zone transverse to the crack ≈ 300–400 µm). Moreover, since the test specimen is only locally damaged, the plastic deformation due to weld fatigue can be observed based on the permanent crack opening—giving deformations of ≈ 35 µm by shear and ≈ 5 µm by pure opening.

The highest magnification revealed that the surface at the crack edges is rich in slip-lines, which typically precede the crack nucleation. Imaging at the fracture surface (Fig. 13, inset on the far right) shows the striations formed by the cyclic load, similarly as in Fig. 9. The crack onset for GE2 specimens occurred at one end of the specimen. However, SEM suggests fatigue damage also at the opposite end of the specimen (Fig. 14). This means that the overall fatigue process is on-going throughout the weld seam in the specimen—though the extent of damage is presumably significantly less at the central area than at the ends where crack onset occurs.

3.4. Numerical weld seam fracture analysis

The VCCT crack simulation was used to describe the final failure process in terms of the local material integrity. The GE2 specimen design was found the most promising design for fatigue testing under shear. The measure for the influence of shear during the fracture process is described by the mode-II dominance at the crack-tip. The mode-

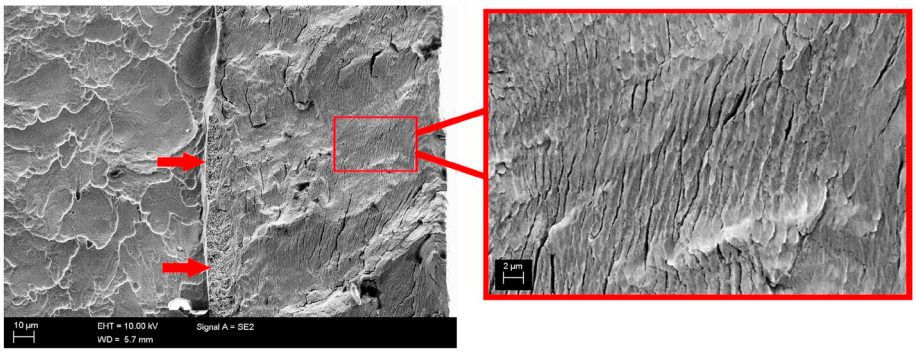

Fig. 9. Detailed SEM imaging of the weld fracture surfaces along the shear part; a GE2 specimen's weld fracture surface near the weld corner (S ≈ 3–4 mm). The red arrows are showing brittle failure at the full depth (root) of weld inside the specimen (between the two halves).

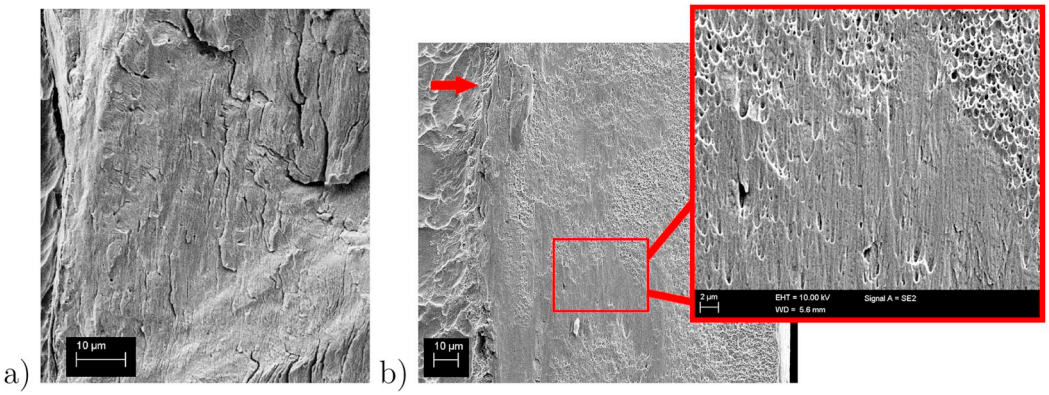

Fig. 10. Detailed SEM images of the weld fracture surfaces along the shear part: a) a GE2 specimen's weld fracture surface at central point (S ≈ 10–12 mm) on the left specimen side; b) a GE2 specimen's weld fracture surface at central point (S ≈ 10–12 mm) on the right specimen side. Images related to a specimen tested with a nominal shear (peak) stress of 32 MPa, after failure (3034 cycles). The red arrow is showing regions of fatigue damage at the weld root.

mixity ($\psi = G_{II}/G_I$) values for 21 different crack lengths are shown in Fig. 15 for the GE2 specimen. It can be seen that the overall failure mode of the specimen does not essentially affect the mode-mixity distribution: The mode-II energy release rate (G_{II}) dominance is clear along the shear part. In detail, for the asymmetric case, where the crack onsets only at one end of the specimen, G_{II} dominance increases for longer cracks (towards the center $S \approx$ 10–12 mm).

The increase (ratio) is higher, the higher is the tensile load applied ($\Delta\psi \approx$12–53% for 1–3 kN, respectively). In the event of simultaneous crack onset at both ends of the specimen, the change in the dominance is opposite but over a lower mode-mixity range ($\Delta\psi \approx$ 10 %). For the preferred asymmetric failure process, the average mode mixity range is $\psi \approx$1.3–1.6 (for 1–3 kN, respectively) for the shear dominated part.

The opening of crack during the final phase of fatigue is driven by the strain energy release at the maximum, peak load level per fatigue cycle. The total ERR values computed for 21 different crack lengths in the GE2 specimen are shown in Fig. 16. It can be seen that the G_{TOT} (i.e. total energy release rate) level increases for longer cracks and it explains the increase in the crack-growth rate during experiments. The increase in the G_{TOT} level for longer cracks is clearly more pronounced for a case where cracks open simultaneously at the both ends of the specimen. This in turn explains the higher variation in the results of the GE1 specimens (Fig. 7) when the crack onset was observed to frequently occur at both ends during the tests of the GE1 specimens.

4. Discussion

The scatter in fatigue results (S–N data) when using the traditional torque specimen can be due to the (1) effect of axial compression/tension that tends to emerge after crack onset, and (2) stiffness and loading changes due to highly asymmetric weld failure. The localization of crack onset is due to the start and end points of the weld seam that is rather impossible to prevent without changing the loading concept of the specimen. The tensile-loaded specimen can be used to circumvent the weld start/end point issue but, in turn, the fatigue process is strongly affected by the pre-crack (i.e. fracture mechanics) and the shear load forms a distribution (Fig. 5) instead of being essentially constant. Practical and device-specific work is needed to study the correspondence between various shear (stress) distributions, the fatigue lives, and the S–N data collected relative to the nominal stress value (mean over the weld contact plane) defined in this study.

An important continuation in the fatigue analysis of CoCr alloys would be to produce S–N data for in-vitro (simulating) conditions. It has been reported that static ultimate failure surfaces in CoCr welds tend to reveal micro-cracks (Baba et al., 2004) due to the mismatch in thermal expansion and following internal residual stresses after welding. This behavior of welds is susceptible to corrosion and can lead to stress-corrosion cracking if subjected to a harsh (in-vitro) environments, such as specific simulated body fluid (SBF) immersion and temperature, along with mechanical loading. In this study, micro-cracks were

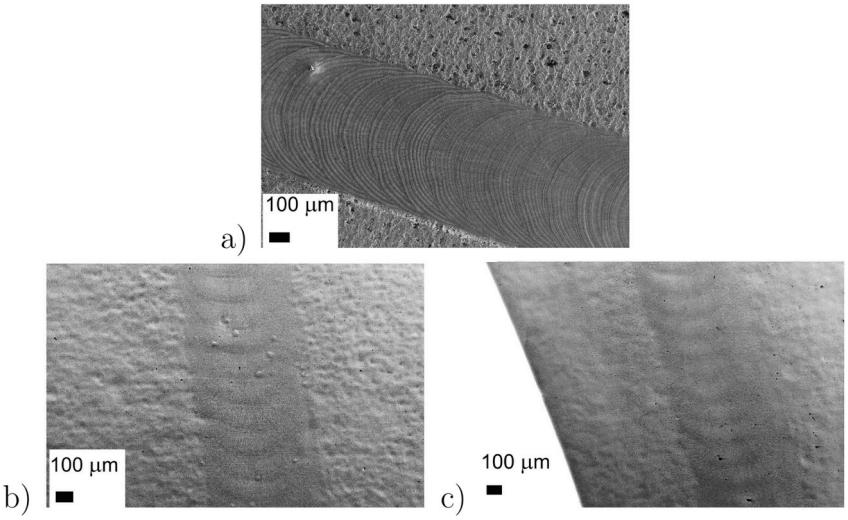

Fig. 11. The urface condition of GE specimens with or without electropolishing (EP): a) no electropolishing; b) electropolished (type GE1); c) electropolished (type GE2).

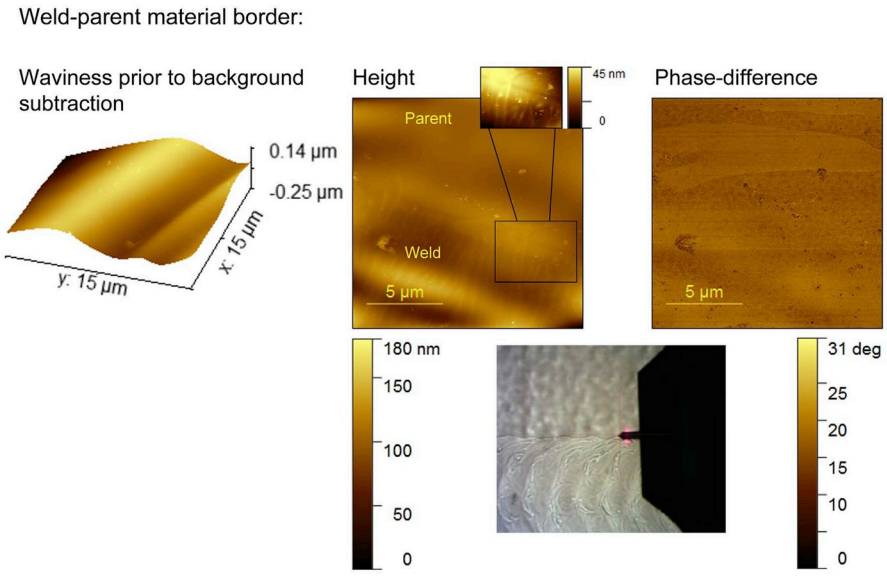

Fig. 12. AFM analysis of the weld-virgin parent material interface showing both parent and weld materials' surface morphology.

observed on fatigue fracture surfaces in addition to striations formed by the crack propagation due to cyclic loading (Fig. 13). However, exact differentiation between fatigue crack evolution and cracking due to internal residual stresses is impossible based on pure imaged data. In general, the original CoCr laser welds and solders for medical applications in the turn of millennia were characterised by large flaws and voids in the weld seam (Srimaneepong et al., 2008; Watanabe et al., 2005) making them mechanically brittle. These flaws in the weld assumably were due to non-optimum welding/soldering parameters or the applied gas atmosphere (Henriques et al., 1997). Here, the weld zone quality in terms of the composition and fracture surface evenness was high compared to many preceding studies emphasizing the essence of preparation on the mechanical properties of laser welds. The exact processes of melting and solidification upon welding control the formation of oxides and carbides at free surfaces, such as at the weld seam root in this study.

Fundamentally, the fatigue damage initiation in the laser weld seam with significant stress and strain gradients (due to bulky parent material pieces) is not clear. Here, we formed a hypothesis that the damage onsets at the weld root, inside the GE specimens, due to the uncontrolled micro-structure and presumed accumulation of contaminants or flaws (Figs. 9 and 10). In this case, the micro cracks propagate towards the outer surface, where intense slip-line accumulation was

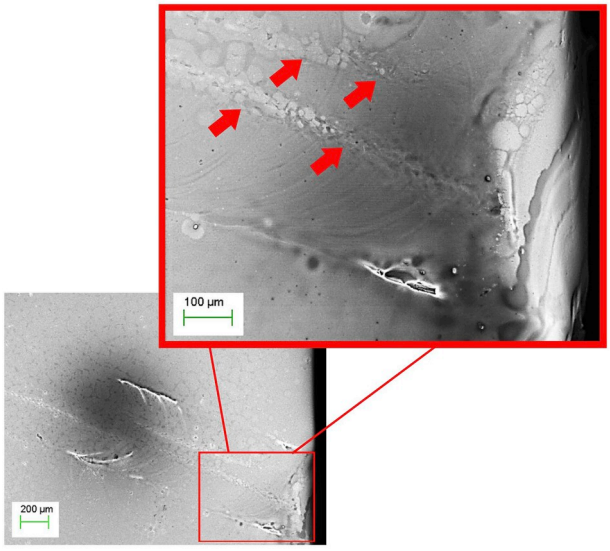

Fig. 14. SEM images of the weld seam at the intact end of a fatigue test specimen after 54 995 cycles (type GE2). The red arrows show the surface damage due to fatigue.)

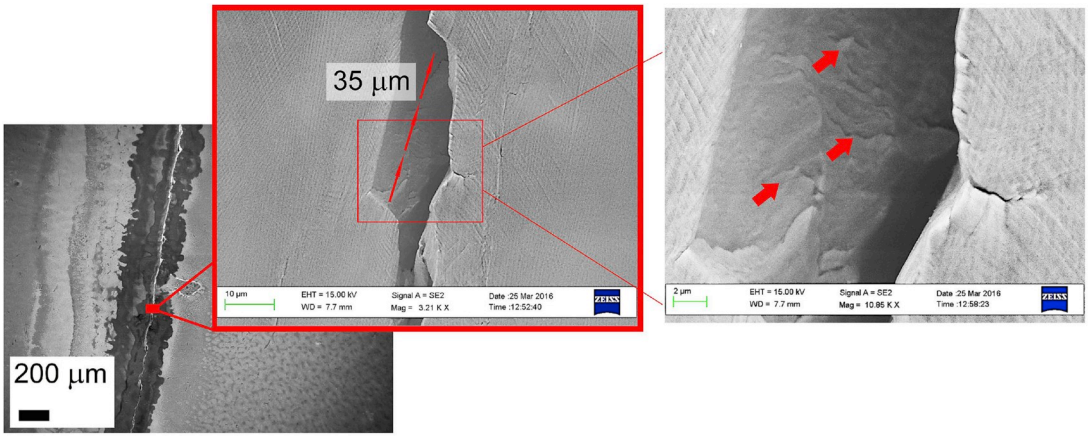

Fig. 13. SEM images of the onset crack in a fatigue test specimen after 27 197 cycles (type GE1). The red arrows show fatigue crack propagation ridges on the fracture surface.

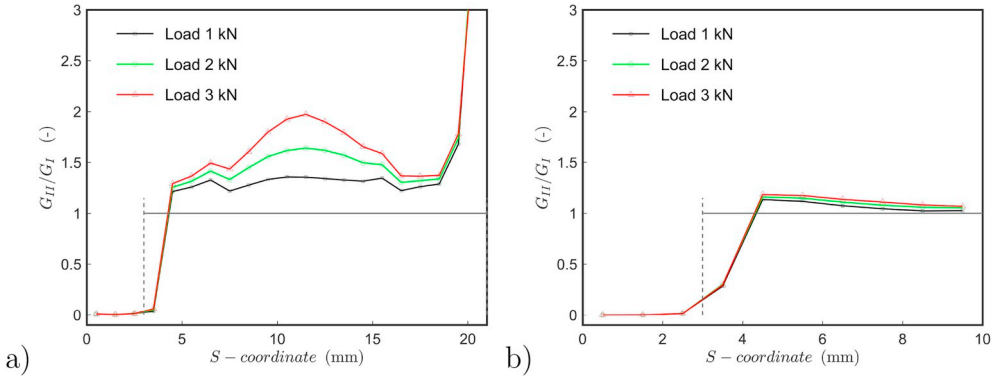

Fig. 15. FEA results on the mode-mixity for different crack lengths: a) crack onset at one end only; b) crack onset at both ends of specimen. Gray lines are showing the shear load dominated part along *S*-coordinate. Note that the curves are symmetric over the $S = 12$ mm point in the symmetric fracture case (b).

observed for different locations and phases of fatigue (Fig. 14). The fatigue testing by using the GE2 specimens led to S–N curves with a typical 'hockey stick' shape, i.e. the plateau of infinite life for low stresses. It is interesting to note that tensile fatigue testing of similar CoCr alloy did not show any clear fatigue limit ('plateau') in the study by Sweeney et al. (Sweeney et al., 2014)—yet it should be noted that the extent of data in their study was low to extrapolate any S–N curve. Complete verification of the fatigue hypothesis would require building a 3-D micro scale finite element model of the weld seam. However, the determination of exact material parameters for the weld, especially in the event of cohesive zones (Gustafson and Waas, 2009; Roy et al., 2007) has shown to be challenging.

The fatigue limit is influenced by the precise 3-D stress-condition (Papadopoulos, 1995; Brown and Miller, 1973), and the triaxiality in the micro scale weld (root) depends on the free space between specimen halves, weld depth, and residual stresses. For a shear-dominated fatigue and fracture, it is important to distinguish between pure shear and simple shear for stress triaxiality (Nielsen and Tvergaard, 2009). In spot welds under global shear (e.g., lap-joint), large strain gradients due to bulky substrates (i.e., small weld spot compared to parent substrates (Nielsen, 2008) lead to a simple shear condition. The difference with the simple shear condition is the amount of hydrostatic tension and the anticipated effects on possible micro-void rotation and coalescence (Tvergaard, 2015)—many of the micromechanical models predict no failure in low or zero triaxiality cases (or are not valid for those). For the developed GE specimens with close to zero moment at test machine grippings, the stress state in the miniature weld seam is considered to be close to simple shear. In turn, the practically necessary tensile or compressive load component when testing the traditional torque-loaded specimen (to keep the force control stable near zero level) leads to a non-simple shear condition. Especially at the time of crack onset in the traditional specimen, the test operator loses the control of exact stress triaxiality and this presumably causes real, though unwanted, scatter in the fatigue test data.

5. Conclusions

In this study, we used hardened cobalt-chromium (CoCr) alloy as a benchmark case. Weld seam specimens were prepared by applying a welding voltage of 175 V, 0.4 mm beam (diameter) and pulse duration of 3 ms. These types of welds are typical for medical devices, such as implants, dentures, and dental prostheses. Finally two candidate specimen designs (designated as GE1 and GE2) were established to compete the rival test method. The GE series specimens were tensile-loaded in order to generate shear loading along the axial portion of the weld seam.

The new-generation specimens resulted in convenient and relatively stable behavior when determining the S–N graph data points for the laser seam material over a 0 … 10^6 load cycle range. The crucial difference compared to the traditional test procedure is the pre-crack formation, which is needed to focus cyclic loading directly to the weld seam. Therefore, fatigue damage concentrated to the welded material yet the entire weld in its length experienced damage prior to the final, fracture-governed failure phase of the weld seam. For the CoCr weld seams here, a conservative fatigue limit of 10.8–11.8 MPa was determined based on a power law regression, where the stress refers to the arithmetic average shear stress level computed along the region dominated by shear loading (fracture mode mixity varies $\psi \approx 1.3$–1.6). Numerical fine-tuning of the new specimen weld process allows adjusting the strain energy release rate during the final fracture phase of the testing, giving potential to further improvement of the new procedure.

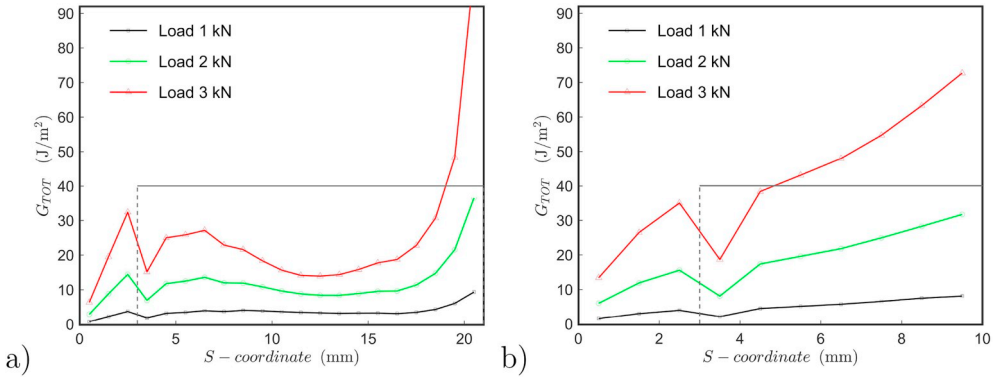

Fig. 16. FEA results on G_{TOT} for different crack lengths: a) crack onset at one end only; b) crack onset at both ends of specimen. Gray lines are showing the shear load dominated part along *S*-coordinate. Note that the curves are symmetric over the $S = 12$ mm point in the symmetric fracture case (b).

Conflicts of interest

There is no conflict of interest related to the results reported in this study.

Acknowledgement

This investigation was funded by a grant from the Ministry of Social Affairs and Health (Finland) and a grant by the Finnish Cultural Foundation through the PoDoCo program. The grant by the ministry was applied in collaboration with Orton Orthopaedic Hospital (9310/405, 9310/448). The authors want to thank Synoste Ltd (Finland) and Mectalent Ltd (Finland) for collaboration during the project and support for analyses and testing; especially researchers R. Livingston and T. Sutinen are acknowledged. Professor Mark Rutland is gratefully acknowledged for his support on the AFM work and suggestions for the test specimen development. CSC IT Center for Science is acknowledged due to their expertise on computation services.

Appendix B. Supplementary data

Supplementary data to this article can be found online at https://doi.org/10.1016/j.jmbbm.2019.07.004.

Appendix A. Detail drawings of three different fatigue test specimens used in the study

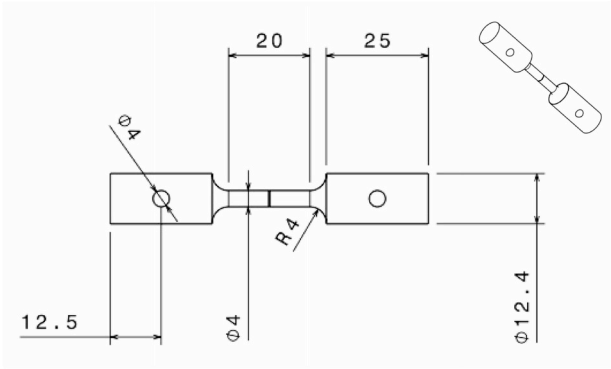

Figure A.17. The traditional torque-loaded fatigue test specimen.

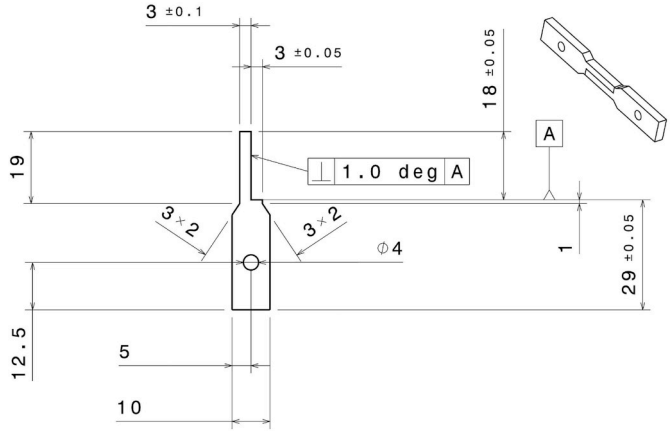

Figure A.18. The suggested tensile-loaded fatigue test specimen designated as GE1.

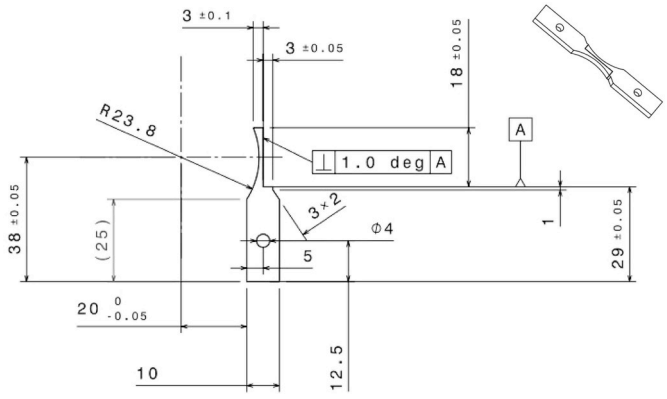

Figure A.19. The suggested tensile-loaded fatigue test specimen designated as GE2.

References

ASTM E8/E8M–09, 2009. Standard Test Methods for Tension Testing of Metallic Materials. ASTM International, West Conshohocken, USA.

Al Jabbari, Y., Koutsoukis, T., Barmpagadaki, X., Zinelis, S., 2014. Metallurgical and interfacial characterization of PFM Co-Cr dental alloys fabricated via casting, milling or selective laser melting. Dent. Mater. 30 (1), e79–e88.

Antunes, R., De Oliveira, M., 2012. Corrosion fatigue of biomedical metallic alloys: mechanisms and mitigation. Acta Biomater. 8 (3), 937–962.

Baba, N., Watanabe, I., Liu, J., Atsuta, M., 2004. Mechanical strength of laser-welded cobalt-chromium alloy. J. Biomed. Mater. Res. Part B App Biomat 69 (2), 121–124.

Baumgart, R., Bürklein, D., Hinterwimmer, X., 2005. 'The management of leg-length discrepancy in Ollier's disease with a fully implantable lengthening nail'. J. Bone Jt. Surg. 87, 1000–1004.

Bertrand, C., Le Petitcorps, Y., Albingre, L., Dupuis, V., 2001. The laser welding technique applied to the non precious dental alloys procedure and results. Br. Dent. J. 190 (5), 255–257.

Bhat, A., Rao, S., Bhaskaranand, K., 2006. Mechanical failure in intramedullary interlocking nails. J. Orthop. Surg. 14 (2), 138–141.

Brown, M., Miller, K., 1973. A theory for fatigue failure under multiaxial stress-strain conditions. Proc. Inst. Mech. Eng. 187 (1), 745–755.

Calder, P., Laubscher, M., Goodier, W., 2017. The role of the intramedullary implant in limb lengthening. Injury 48S (1), S52–S58.

Chang, B., Shi, Y., Lu, L., 2001. Studies on the stress distribution and fatigue behavior of weld-bonded lap shear joints. J. Mater. Process. Technol. 108 (3), 307–313.

Gustafson, P., Waas, A., 2009. The influence of adhesive constitutive parameters in cohesive zone finite element models of adhesively bonded joints. Int. J. Solids Struct. 46 (1), 2201–2215.

Hedberg, Y., Qian, B., Shen, Z., Virtanen, S., Odnevall Wallinder, I., 2014. In vitro biocompatibility of CoCrMo dental alloys fabricated by selective laser melting. Dent. Mater. 30 (5), 525–534.

Henriques, G., Consani, S., Rollo, J., Andrade e Silva, F., 1997. Soldering and remelting influence on fatigue strength of cobalt-chromium alloys. J. Prosthet. Dent 78 (2), 146–152.

Hryniewicz, T., Rokicki, R., Rokosz, K., 2008. 'Co-Cr alloy corrosion behaviour after electropolishing and "magnetoelectropolishing" treatments'. Mater. Lett. 62 (17–18), 3073–3076.

Kanerva, M., Besharat, Z., Livingston, R., Rutland, M., Göthelid, M., 2015. Plasticity effects during the 4-point bending of intramedullary leg lengthening implants with telescopic structures. In: 6th International Conference on Mechanics and Materials in Design (Proceedings)', Ponta Delgada, Portugal. July 26-30.

Kanerva, M., Besharat, Z., Pärnänen, T., Jokinen, J., Honkanen, M., Sarlin, E., Göthelid, M., Schlenzka, D., 2019. Automatization and stress analysis of CoCr laser weld fatigue tests. Data in Brief Submitted for publication.

Krueger, R., 2004. Virtual crack closure technique: history, approach, and application. Appl. Mech. Rev. 57 (2), 109–143.

Ladani, L., Dasgupta, A., 2009. A meso-scale damage evolution model for cyclic fatigue of viscoplastic materials. Int. J. Fatigue 31 (4), 703–711.

Lee, S., Lai, J., 2003. The effects of electropolishing (ep) process parameters on corrosion resistance of 316l stainless steel. J. Mater. Process. Technol. 140 (1–3 SPEC), 206–210.

Limmahakhun, S., Oloyede, A., Sitthiseripratip, K., Xiao, Y., Yan, C., 2017. Stiffness and strength tailoring of cobalt chromium graded cellular structures for stress-shielding reduction. Mater. Des. 114, 633–641.

Mani, G., Feldman, M., Patel, D., Agrawal, C., 2007. Coronary stents: a materials perspective. Biomaterials 28 (9), 1689–1710.

Marrey, R., Burgermeister, R., Grishaber, R., Ritchie, R., 2006. Fatigue and life prediction for cobalt-chromium stents: a fracture mechanics analysis. Biomaterials 27 (1), 1988–2000.

Nielsen, K., 2008. Ductile damage development in friction stir welded aluminum (AA2024) joints. Eng. Fract. Mech. 75 (10), 2795–2811.

Nielsen, K., Tvergaard, V., 2009. Effect of a shear modified Gurson model on damage development in a FSW tensile specimen. Int. J. Solids Struct. 46 (1), 587–601.

Okyar, A., Bayoglu, R., 2012. The effect of loading in mechanical response predictions of bone lengthening. Med. Eng. Phys. 34 (9), 1362–1367.

Papadopoulos, I., 1995. A high-cycle fatigue criterion applied in biaxial and triaxial out-of-phase stress conditions. Fatigue Fract. Eng. Mater. 18 (1), 79–91.

Radaj, D., 1990. Design and Analysis of Fatigue Resistant Welded Structures. Woodhead Publishing, UK1855730049.

Roy, S., Darque-Ceretti, E., Felder, E., Monchoix, H., 2007. Cross-sectional nanoindentation for copper adhesion characterization in blanket and patterned interconnect structures: experiments and three-dimensional FEM modeling. Int. J. Fract. 144 (1), 21–33.

Scholz, R., Knyazeva, M., Porchetta, D., Wegner, N., Senatov, F., Salimon, A., Kaloshkin, S., Walther, F., 2018. Development of biomimetic in vitro fatigue assessment for UHMWPE implant materials. J. Mech. Behav. Biomed. Mater. 85, 94–101.

Srimaneepong, V., Yoneyama, T., Kobayashi, E., Doi, H., Hanawa, T., 2008. Comparative study on torsional strength, ductility and fracture characteristics of laser-welded α + βTi-6Al-7Nb alloy, CP titanium and Co-Cr alloy dental castings. D*ent. Mater.* 2**4** (6), 839–845.

Sweeney, C., O'Brien, B., McHugh, P., Leen, S., 2014. Experimental characterisation for micromechanical modelling of CoCr stent fatigue. Biomaterials 35 (1), 36–48.

Thonse, R., Herzenberg, J., Standard, S., Paley, D., 2005. Limb lengthening with a fully implantable, telescopic, intramedullary nail. Operat. Tech. Orthop. 15, 355–362.

Tiefenboeck, T., Zak, L., Bukaty, A., Wozasek, G., 2016. 'Pitfalls in automatic limb lengthening—first results with an intramedullary lengthening device'. Orthop. Traumatol. v 102 (7), 851–855.

Tvergaard, V., 2015. Study of localization in a void-sheet under stress states near pure shear. Int. J. Solids Struct. 75 (1), 134–142.

Watanabe, I., Benson, A., Nguyen, K., 2005. Effect of heat treatment on joint properties of laser-welded Ag-Au-Cu-Pd and Co-Cr alloys. J. Prosthodont. 14 (3), 170–174.

Zupancic, R., Legat, A., Funduk, N., 2006. Tensile strength and corrosion resistance of brazed and laser-welded cobalt-chromium alloy joints. J. Prosthet. Dent 96 (4), 273–282.